Catalysis Science & Technology

Accepted Manuscript

ROYAL SOCIETY OF CHEMISTRY

www.rsc.org/catalysis

Hydroxyl radical generation by cactus like copper oxide nanoporous carbon catalysts for microcystin-LR environmental remediation

S. Karthikeyan[a], Dionysios D. Dionysiou[b], Adam F. Lee[c], S. Suvitha[a] , P. Maharaja[a], Karen Wilson[c] , G. Sekaran[a*]

a. Environmental Technology Division, Council of Scientific and Industrial Research (CSIR) - Central Leather Research Institute (CLRI), Adyar, Chennai-600 020, Tamilnadu, India.

b. Environmental Engineering and Science Program, University of Cincinnati, Cincinnati, Ohio 45221-0012, United States

c. European Bioenergy Research Institute, Aston University, Aston Triangle, Birmingham B4 7ET, United Kingdom

*** Corresponding Author**

Dr. G. Sekaran,

Chief Scientist & Cluster chairman

Environmental Technology Division,

Central Leather Research Institute,

Adyar, Chennai – 600 020,

Tamil Nadu, India

Tel.: +91-44-24911386 (Extn: 7141)

Fax: +91-44-24452941

Email: ganesansekaran@gmail.com

Abbreviations

APHA	American Public Health Association
AOPs	Advanced oxidation processes
NPAC	Nanoporous Activated Carbon
CuO-NPAC	Copper oxide copper oxide incorporated on nanoporous activated carbon
MC-LR	Microcystin-LR
BET	Brunauer-Emmett-Teller
HK	Horvath Kawazoe
XPS	X-ray Photoelectron Spectroscopy
HR-TEM	High resolution-Transmission Electron Microscopy
HR-SEM	High resolution-Scanning Electron Microscope
XRD	X-Ray Diffraction
EPR	Electron Paramagnetic Resonance
EDX	Energy-Dispersive X-ray spectroscopy
ICP-OES	Inductively Coupled Plasma Atomic Emission Spectroscopy
ROS	Reactive Oxygen Species
HTPA	2-Hydroxyterephthalic acid
DMPO	5,5-Dimethyl-1-pyrroline N-oxide

Abstract

Copper oxide supported on nanoporous activated carbon (CuO-NPAC) is reported for the aqueous phase catalytic degradation of cyanotoxin microcystin-LR (MC-LR). The loading and spatial distribution of CuO throughout the NPAC matrix strongly influences catalytic efficiency. CuO-NPAC synthesis was optimized with respect to the copper loading and thermal processing, and the physicochemical properties of the resulting materials characterized by XRD, BET, TEM, SEM, EPR, TGA, XPS and FT-IR spectroscopy. EPR spin trapping and fluorescence spectroscopy evidenced in situ $^{\bullet}OH$, formation via H_2O_2 over CuO-NPAC as the catalytically relevant oxidant. The impact of reaction conditions, notably CuO-NPAC loading, H_2O_2 concentration and solution pH, are discussed in relation to the reaction kinetics for MC-LR remediation.

Keywords: Heterogeneous Fenton, CuO-NPAC/H_2O_2, Microcystin-LR oxidation, EPR, Fluorescence spin trapping

INTRODUCTION

Microcystins (MCs) are cyanotoxins reported to pose health hazards to animals and humans. Amongst microcystins, microcystin-LR (MC-LR) is identified as one of the most toxic contaminants present in water resources [1, 2]. The stability, and hence biological lifetime, of MCs arises from strong amide bonds within the cyclic heptapeptide unit (see Scheme 1 chemical structure of MC-LR).

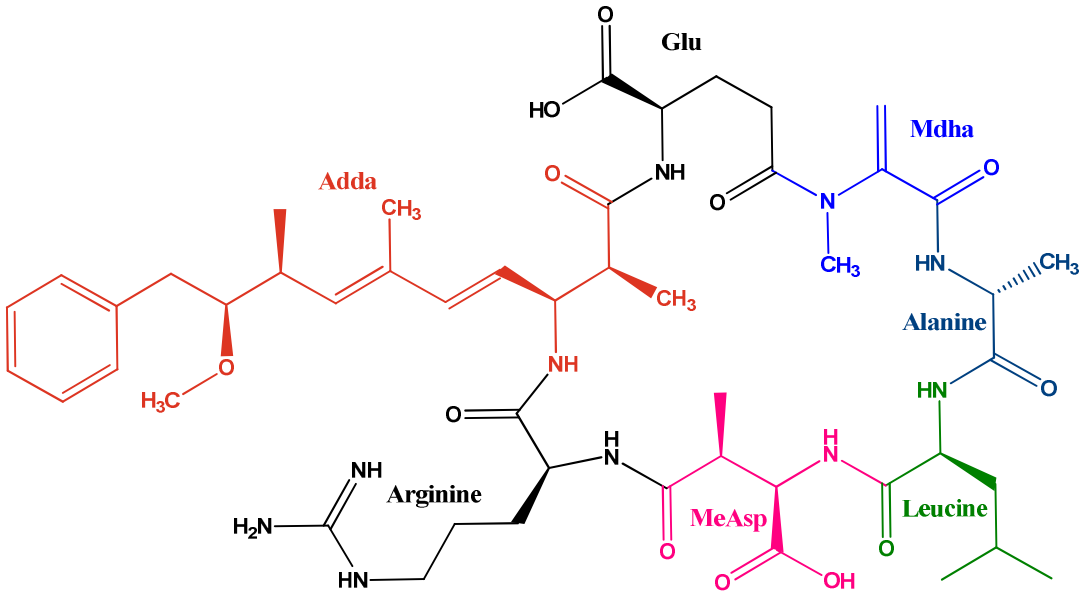

Scheme 1. Different functional groups within MC-LR, notably adda, mdha and amino acids.

Over 80 MC isoforms with similar structures have been reported [3]. The toxicity of MC-LR is associated with the adda functional group [4]. The World Health Organization (WHO) has recommended a provisional concentration limit for MC-LR of 1 $\mu g.L^{-1}$ in drinking water. Physical, chemical and biological treatment methods have been proposed to remove or degrade MC-LR in aqueous solution [5, 6]. Advanced oxidation processes (AOPs) have been considered as promising treatment technologies for MC-LR removal. These include Fenton and photo-Fenton oxidation [6, 7], UV, solar and visible photocatalytic oxidation in the presence of TiO_2 [8-10], and ozonation [11]. Such AOPs lead to

mineralization of the refractory organic compounds, and are mainly based upon the generation of highly oxidizing hydroxyl radicals.

Highly energetic radicals such as $^{\bullet}OH$, $^{\bullet}OOH$, $^{\bullet}O_2^-$ and $^{\bullet}SO_4^-$, have been generated by various AOPs for the destruction of refractory organic compounds in water. Fenton oxidation of organics in water and wastewater has been extensively studied,[12] with the removal of refractory organic chemicals by Fenton type oxidation employing CuO with H_2O_2 has received significant attention in recent years due to its low cost and high efficiency [13]. Recently, Liao et al. reported the oxidative degradation of methylene blue by a CuO/H_2O_2 system with high catalytic activity, reusability and durability[14]. Catalytic decolorization of bromcresol green, crystal violet, methyl red dyes was also demonstrated using the CuO/H_2O_2 system[15], while $CuO\text{-}Al_2O_3$ proved an effective Fenton-like catalyst under microwave irradiation for p-nitrophenol degradation with good stability and reusability[16]. However, Fenton oxidation suffers certain disadvantages, including the generation of metal hydroxide sludge at the pH of natural waters. The shortcomings of homogeneous Fenton oxidation could be overcome by two approaches: (i) providing a porous conductive substrate, e.g. activated carbon, to accept an electron from hydroxyl ions and thereby produce hydroxyl radicals, and/or (ii) providing a supporting matrix to avoid precipitation of metal ions as described for textile, tannery and saline wastewater[17-20]. However, MC-LR removal from aqueous solution at weakly acidic and/or neutral pH has not been adequately studied, and there are no previous reports on heterogeneous catalytic Fenton oxidation of MC-LR using CuO, a p-type semiconductor with a narrow (visible light) band, in conjunction with nanoporous activated carbon (NPAC).

Heterogeneous Fenton oxidation offers an economically and ecologically feasible technology to destroy deleterious organics in surface drinking water supplies without

sludge generation. Here we evaluate the potential of CuO/NPAC heterogeneous catalysts for MC-LR oxidation in aqueous solution.

Materials and methods

Materials and methods are presented in the supporting information.

Results and discussion

Catalyst characterization

Porosimetry

Textural properties, specifically mesopore/micropore/BET surface areas, micro/BJH/total pore volumes, and mesopore diameter are presented in Table 1. BET surface areas decreased following CuO impregnation and subsequent annealing up to 400 ^{o}C. Higher temperatures recovered surface areas close to the parent NPAC value; surface areas (total, mesopore and micropore) were lowest for the CuO-NPAC$_{400}$ matrix.

Adsorption-desorption isotherms of NPAC and CuO-NPAC materials are presented in Fig. 1a. Mean mesopore sizes for NPAC and CuO-NPAC were around 3-5 nm (Fig. S1a) and independent of annealing temperature. Total pore volumes also decreased after copper oxide incorporation, irrespective of annealing temperature. The loss of surface area and pore volume were consistent with the localisation of CuO within the carbon nanoporous network[21]. Copper nitrate decomposition and concomitant copper oxide formation occurred around 300 ºC. Higher annealing temperatures may be anticipated to result in CuO crystallite growth and pore blockage, hence the unexpected rise in surface area at 500 ^{o}C may reflect disruption of the NPAC structure and resulting pore enlargement into the mesopore range[22], consistent with partial decomposition to elemental copper metal and sintering[23]. XPS was employed to elucidate the copper

oxidation state, and Fig. S1b shows the characteristic Cu(II) state around 934 eV binding energy accompanied by an asymmetric satellite at approximately 944 eV following a 500 ^{o}C anneal; consistent with literature reports for CuO formation from the nitrate [23].

Microstructure and elemental composition of catalyst

Light element compositions of the parent NPAC and CuO loaded materials are presented in Table 2, and show a significant rise in the C/N ratio for CuO supported activated carbon with increasing annealing temperature, reflecting a loss of nitrate groups from both the pre-functionalized NPAC support (oxidized with nitric acid to introduce surface functionality) and incorporated copper nitrate. CHNS analysis of NPAC and CuO-NPAC showed high elemental carbon, hydrogen, nitrogen and sulphur contents. The presence of nitrogen and sulphur in NPAC and CuO-NPAC may be arise from the raw material, rice husk, employed in the pyrolytic synthesis of the carbon support; such non-carbon constituents may be advantageous in providing useful surface functionality[24]. CHNS analysis also evidenced an increase in volatile species as a result of the HNO_3 oxidation pretreatment, which our previous XPS studies[17, 19] indicate are associated with surface pyridone groups and amine/amide species with respective binding energies of 401.0 eV and 398 eV. Such nitrogen containing surface functionalities on the NPAC support decompose above 400 °C[25, 26].

Powder XRD patterns of the parent NPAC and CuO-NPAC materials are shown in Fig. 1b, which reveal strong reflections at 26.7º, associated with the aromatic planes in the graphite-like porous NPAC reported in our previous work[17, 19]. XRD patterns of the CuO-NPAC annealed at different temperatures (300-500 °C) showed a broad peak at 24º, indicative of an amorphous phase[27], accompanied by diffraction peaks at 36.9º, 39.8º, 50.64º, 60.4º and 68.6º characteristic of monoclinic CuO for the 300 and 400 °C annealed

samples[28, 29]. Volume averaged crystallite sizes for the CuO phase determined from the Scherrer equation were around 75 nm. Bulk CuO is reported to undergo decomposition above 400 °C[30], and indeed XRD showed no evidence for crystalline CuO after annealing at temperatures >500 °C, wherein it is likely that complete decomposition to metallic copper occurred.

DRUVS Spectroscopy

CuO-NPAC exhibited UV-vis absorption peaks at 230 nm, 329 nm and 350-800 nm (Fig. 1c). The broad absorption band spanning at 400-800 nm is assigned to the porous activated carbon[31], while those features below 400 nm are indicative of copper oxide[32]. The absorption peak at 329 nm showed no blue shift relative to bulk CuO, consistent with the presence of large particles observed by XRD[33].

Fourier Transform Infrared spectroscopy (FT-IR)

FT-IR spectra of NPAC and CuO-NPAC$_{400}$ are presented in Fig. 1d for different Cu loadings. The spectrum of the parent NPAC showed a broad peak at 3441 cm^{-1}, likely due to the presence of N-H stretches in the nitric acid functionalised NPAC. Shoulder bands observed at 2850 and 2924 cm^{-1} were assigned to symmetric and asymmetric C-H stretches arising from aliphatic CH, CH_2, and CH_3 functional groups in NPAC[34]. Another peak at 1622 cm^{-1} is characteristic of carbons, and possibly due to carbonyl functional groups which are highly conjugated in the graphene layer such as quinone and/or ionoradical moities C=O[25]. The broad, weak peak at 1075 cm^{-1} is attributed to C-O stretches of phenolics. Spectra of CuO-NPAC materials also showed absorption peaks at 526 cm^{-1}, attributed to CuO stretches[35] from nanoparticles within the NPAC matrix. The

N-H stretching frequency was also shifted relative to the parent NPAC to 3428 cm^{-1}, probably due to the interaction of nitrogen lone pairs with CuO within the NPAC matrix.

Thermogravimetric Analysis (TGA)

TGA profiles of as-prepared NPAC and CuO-NPAC were performed between 30 ºC to 800 ºC under a N_2 atmosphere to evaluate the catalyst thermal stability. Thermograms of NPAC and CuO-$NPAC_{300,}$ CuO-$NPAC_{400,}$ and CuO-$NPAC_{500}$ are presented in Fig. 2a. A common 7 % mass loss was observed from 100-180 ^oC due to desorption of physisorbed and chemisorbed water from the NPAC and CuO-NPAC materials[21]. Further significant mass losses of 6.3 % and 12.8 % were observed between 390-502 ºC for CuO-$NPAC_{400}$ and CuO-$NPAC_{500}$ respectively, attributed to the decomposition of surface functions from the carbon matrix[17]. Larger mass losses of 18.8 % and 34.7 % occurred between 500-800 ºC for CuO-$NPAC_{400}$ and CuO-$NPAC_{500}$ respectively, attributed to pyrolysis of the carbon support[36]. The observation that CuO-$NPAC_{400}$ was more stable than CuO-$NPAC_{500}$ may reflect activation of the carbon matrix during the material pre-processing. Fig. 2b illustrates the thermal stability of CuO-$NPAC_{400}$ for different CuO loadings (0.1-2.0 wt.%). These thermograms revealed a 7.4 % mass loss around 230 ºC and 14.3 % mass loss around 450 ºC due to surface functional groups on the carbon matrix as reported by Wang et al[37]. Compared with NPAC, CuO-NPAC showed a total mass loss of 73 % by 800 ºC, compared with 65.8 % for the support, i.e. NPAC exhibited poorer thermal stability following CuO incorporation, presumably due to the catalytic effect of CuO in activating the support[38].

X-Ray Photoelectron Spectroscopy of NPAC and CuO-NPAC

XPS was performed to determine the oxidation state and composition of the CuO-NPAC materials (Fig. 3). The high-resolution core level C 1s spectrum showed a strong feature at 284.5 eV binding energy indicative of amorphous carbon (284.2–285.5 eV)[39]. The state at 286.3 eV is assigned to C-OH functions from epoxide and hydroxyl groups on the NPAC matrix. The O 1s core level spectrum (Fig. 3b) was broad and asymmetric, indicating the presence of multiple oxygen species, with peak fitting revealing components at 530.3 eV and 532.4 eV, the former attributed to CuO and the latter to oxygenates in the carbon matrix (Fig. 3b). Fig. 3c shows a survey spectra of CuO-NPAC. The Cu $2p_{3/2}$ feature at 933.6 eV is characteristic of CuO[34], with corresponding shake-up satellites at 940.1-943.1 eV [40, 41].

EPR Spectra of NPAC and CuO-NPAC$_{400}$

EPR spectra confirmed the paramagnetic behaviour of NPAC and CuO-NPAC matrices[42]. Fig. 4 shows the EPR spectra of CuO-NPAC at different annealing temperatures. The EPR spectra were recorded for NPAC, CuO-NPAC$_{300}$, CuO-NPAC$_{400}$, and CuO-NPAC$_{500}$. Fig. 5 presents the EPR spectra of CuO-NPAC for different copper oxide loadings in NPAC matrix. However, the intensities of the signals were very weak, attributed to a low concentration of oxygen vacancies and lattice defects in the CuO-NPAC matrix[43]. The EPR results show that copper was present as Cu^{2+} with an outer shell configuration of $3d^9$. Unpaired electrons in the NPAC matrix arise from delocalization of π-bonded electrons in the conjugated carbon matrix during carbonization[44].

The 'g' factors calculated from EPR spectra are presented in Table 3. The principal g values calculated using the formula $g = h\nu/B\beta$ are consistent with the reported

distorted octahedral environment of Cu(II) ion. Bulk CuO is ESR silent, whereas both dispersed CuO and isolated Cu(II) sites are ESR active, and the signal intensities were affected by the presence of these neighboring species[32]. The lower signal intensity observed for CuO-NPAC (1.0 wt.%) indicates a higher quantity and dispersion of CuO or Cu(II) species in the NPAC matrix. It is clear that the g value of NPAC is very high compared to conventional supported copper oxide catalysts, i.e. the g value decreased when copper oxide was incorporated into the NPAC support. Moreover, the generation of hydroxyl radicals from CuO-NPAC was confirmed by EPR spin trapping. Fig. S2a shows a typical four line EPR spectrum as monitored using Fenton oxidation system.

Fig. S2b presents the EPR spectrum of CuO-NPAC$_{400}$, showing solid EPR spectral lines of the DMPO-$^{\bullet}$OH adduct (presented in redline). The generation of $^{\bullet}$OH and $O_2^{\bullet-}$ (Reactive Oxygen Species; ROS) radicals using DMPO was determined by ESR, with DMPO-$^{\bullet}$OH and DMPO-$O_2^{\bullet-}$ observed for CuO-NPAC/H_2O_2 system. Fig. S3a-b (Supporting information) show the photoluminescence spectra of NPAC and CuO-NPAC matrices.

Photoluminescence (PL) spectra were recorded at different excitation wavelengths for NPAC and CuO-NPAC. NPAC showed features for excitation wavelengths between 320 nm to 410 nm, whereas CuO-NPAC only exhibited excitation at 390 nm. This clearly shows that these PL bands are not due to band gap emission, but rather attributed to various structural defects in the matrix. As presented in Fig. S3a-b, CuO-NPAC showed strong emission peaks at 432.8 nm (2.86 eV), 458.8 nm (2.7 eV), and 484.9 nm (2.55 eV), while NPAC showed intense emission peaks at 399 nm (3.11 eV), 434.6 nm (2.85 eV), and 529.3 nm (2.34). These emission peaks are generated due to structural defects, such as oxygen vacancies in the matrix[45]. Oxygen vacancies on the surface of NPAC and CuO-NPAC would favor O_2 adsorption and subsequent generation

of reactive oxygen species, with consequent oxidation of organic compounds. Thus, NPAC and CuO-NPAC, with structural defects and oxygen vacancies on its surface, would seem a promising catalyst for the oxidation of organic compounds in wastewater.

Scanning Electron Microscopy of NPAC and CuO-NPAC$_{400}$

Scanning Electron Microscopy images of NPAC and CuO-NPAC$_{400}$ are presented in Fig. 6a-c and Fig. 6e-k, respectively. The copper oxide exhibited cactus like structure of 1-5 μm diameter. EDX analysis of NPAC and CuO-NPAC are presented in Fig. 6d and Fig. 6i, respectively. Fig. 6i verifies the presence of copper in the NPAC matrix. The SEM image clearly shows that the CuO-NPAC cactus like structure is highly porous. This suggests that CuO-NPAC comprises nanosize fine particles integrated within carbon layers. Plugging of the nanoporous activated carbon support by CuO nanoparticles accounts for the loss of micropore area; these particles appear regularly oriented. The porous structure reflects chemical activation during acid pretreatments[46].

High-resolution Transmission Electron Microscopy analysis of NPAC and CuO-NPAC$_{400}$

The formation of cactus like nanospheres was investigated using transmission electron microscopy (HR-TEM). The digitized original HR-TEM images of CuO-NPAC are shown Fig. 7**.** HR-TEM of CuO-NPAC$_{400}$ provides an indication of graphitic layers embedded in the amorphous NPAC matrix (Fig. 7a), with lattice planes of 0.19 nm and 0.23 nm, consistent with the XRD derived lattice parameters[47]. The SAED pattern of CuO-NPAC (Fig. 7, inset on the upper left) confirms CuO was embedded in the NPAC matrix. As presented in Fig.7c, the elemental composition of CuO-NPAC$_{400}$ was confirmed through EDX spectral analysis of CuO-NPAC$_{400}$. The presence of graphitic

nature of NPAC is revealed in the HR-TEM image presented in Fig.7d. The origin of the pores may be attributed to the defect sites created during growth of CuO nanocrystallites in the carbon matrix. CuO nanoparticles were uniformly distributed in the carbon network with mean particle diameters between 5 to 20 nm (Fig. 8a-l). The figure shows that a large number of cactus-like copper oxide particles were bound in the external spheres of nanoporous activated carbon associated with void formation. The zones of black dots are considered to be the voids in the CuO nanoparticle of CuO-NPAC$_{400}$. The CuO loading in NPAC and leaching after MC-LR oxidation was estimated by ICP-OES (Table S1), and evidences negligible copper dissolution in-situ in all cases.

Degradation of MC-LR using CuO-NPAC

Rate constants for MC-LR degradation over different CuO-NPAC materials in the heterogeneous Fenton oxidation process are presented in Table S1. The reaction kinetics fitted well to a first-order reaction model with a regression coefficient of 0.97. Rate constants exhibited only a weak dependence on CuO loading, varying from 2.93×10^{-2} min^{-1} for 0.086 wt.% CuO to 4.26×10^{-2} min^{-1} for 1.56 wt.% CuO, indicating that the maximal rate of hydrogen peroxide decomposition was attained over relatively small and highly-dispersed CuO nanoparticles. Additional MC-LR degradation reactions were performed using 1 wt.% CuO in NPAC. Fig. 9a shows the degradation of MC-LR at different time intervals for four different catalytic systems: (i) 1 wt.% FeO and 15 mM H_2O_2; (ii) 1 wt.% CuO and 15 mM H_2O_2; (iii) 2 g/L CuO-NPAC; and (iv) 2 g/L CuO-NPAC and 15 mM H_2O_2. MC-LR degradation of 96% was achieved after 80 min using the heterogeneous Fenton oxidation process (CuO-NPAC$_{400}$ with H_2O_2) while only 60 % degradation was obtained using iron oxide or copper oxide alone with hydrogen peroxide. By contrast, Bandala et al. reported maximal MC-LR degradation of only 20

% after 600 min using 0.5 mM of H_2O_2 and 0.25 mM of iron (II) species,[48] requiring higher H_2O_2 concentrations (2.5–5 mM) to attain significant degradation levels of 61 % in 180 min.[49] In the present study, use of our heterogeneous Fenton oxidation process combing CuO-$NPAC_{400}$ with H_2O_2 clearly offers superior MC-LR degradation. A set of experiments was also carried out in the presence of only CuO-NPAC without H_2O_2 to determine the extent of MC-LR removal due to adsorption. The reduction in MC-LR concentration due to adsorption was only 10-27% in all cases. Figs. 9b and 9c show the UV-Vis spectral analysis of the MC-LR reaction mixture before and after heterogeneous Fenton oxidation process. The UV–Visible spectrum of MC-LR presented characteristic bands at 238 nm[50] attributed to the presence of aromatic C=C bonds and associated π–π* transition. The UV–Vis spectrum of MC-LR after heterogeneous Fenton oxidation process using CuO-NPAC/H_2O_2 confirmed that the 238 nm peak intensity was substantially reduced due to decomposition of the C=C bond in the Adda region and associated MC-LR destruction.

FT-IR spectra to confirm the oxidation/destruction of MC–LR

Fig. 9d presents FT-IR spectra of MC–LR before and after reaction with different catalytic oxidation systems. Fig. 9d shows characteristic bands of MC-LR, with a peak at 3445 cm^{-1} due to N-H stretching in MC-LR, and peaks at 3046 cm^{-1} and 2928 cm^{-1} due to aliphatic and aromatic C-H functional groups. Peaks at 1642 cm^{-1}, 1437 cm^{-1} and 1132 cm^{-1} are also attributed to aromatic C=C and C=N stretches in MC-LR. Degradation was observed following different catalytic oxidations. As shown in Fig. 9d, the characteristic peaks of MC-LR shifted and became broader which may be due to the formation of oxidized products of MC-LR.

Effect of pH on MC-LR degradation

Solution pH is often one of the most important operating variables influencing the performance of heterogeneous catalytic oxidation process, hence MC-LR degradation was explored at initial pH values of 3, 7 and 9 under the following conditions: 2 g/L CuO-NPAC; 15 mM H_2O_2; 80 min reaction time; 50 µg/L initial MC-LR concentration. Fig. 10a shows that the resultant MC-LR concentration was reduced by 98%, 95.4% and 94% at pH 3, 7 and 9 respectively after 80 min reaction, demonstrating the versatility of our CuO-NPAC catalyst over a wide pH range[51, 52].

Influence of initial MC-LR concentration

Fig. 10b shows the percentage removal of MC-LR as a function of initial reactant concentration (10 µg/L, 25 µg/L, 50 µg/L or 100 µg/L) in the CuO-NPAC/H_2O_2 system at a common initial 15 mM peroxide concentration. The initial rate of MC-LR degradation increased from $3.2x10^{-2}$ µg.min^{-1} to $5.6x10^{-2}$ µg.min^{-1} with increasing MC-LR concentration from 10-100 µg/L. The weak positive order in MC-LR molecules suggests that degradation is largely rate-controlled by H_2O_2 production over CuO-NPAC rather than the rate of oxidation of MC-LR by resulting radicals, with an excess of [$^{\bullet}$OH] present at ambient temperature accounting for the high 60 min conversion levels (91-97%) observed for initial MC-LR concentrations of 25-100 µg/L. The pseudo-first-order rate constant for MC-LR degradation decreased slightly with initial MC-LR concentration from $k=4.6 \times 10^{-2}$ min^{-1} for 10 µg/L initial MC-LR to 3.8×10^{-2} min^{-1} (50 µg/L) and $k=2.9 \times 10^{-2}$ min^{-1} for 100 µg/L. The decrease at high MC-LR concentration may reflect the formation of significant metastable intermediate fragments during the heterogeneous Fenton oxidation process. At high MC-LR concentrations the

accumulation of degradation products within the CuO-NPAC matrix may hinder mass transport and the resultant catalyst efficiency. Antoniou et al.[57] reported photocatalytic degradation of MC-LR and intermediates formation over TiO_2 and proposed that conjugated diene bonds were the most reactive molecular functions with respect to hydroxyl radicals. Such a mechanism accounts for the formation of multiple organic by-products during MC-LR degradation, which undergo stepwise attack by hydroxyl radicals.

Influence of hydrogen peroxide

Fig. 10c shows the removal of MC-LR at different H_2O_2 concentrations (5 to 25 mM) by CuO/NPAC. In this series of experiments, the initial MC-LR concentration was fixed at 50 µg/L. MC-LR degradation increased with H_2O_2 concentration up to 15 mM, catalytic efficiency decreasing slightly thereafter at higher peroxide concentration. Hydrogen peroxide has long been used for the degradation of refractory organics in aqueous media, with the degradation rate reported to decrease at high peroxide concentrations due to scavenging of hydroxyl radicals by excess unreacted H_2O_2[53 54].

The recyclability of CuO-$NPAC_{400}$ was evaluated in batch degradation under optimum conditions: reusability, stability, and durability of CuO-$NPAC_{400}$ catalyst are key factors for assessing its long term performance. Our experiments revealed that CuO-$NPAC_{400}$ could be reused five times with no loss of catalytic efficiency (Fig. 10d).

Proposed mechanism for hydroxyl radical generation

The copper oxide in NPAC showed O_2 and N_2 containing functional groups in NPAC, and the unpaired electrons of copper oxide show paramagnetic nature (confirmed through EPR spectral analysis with g factor value ~2.3) [55]. The crystal field splitting

energy is very high (fluorescence spectra in Fig. S3b show strong emission at 390 nm) and this is attributed to the presence of free electrons. The free electrons initiate the formation of hydroxyl radicals from H_2O_2. The generation of hydroxyl radical was confirmed using terephthalic acid method [56] as shown in the results presented in Fig. S4. Pictorial representation and mechanistic view of CuO-NPAC$_{400}$ to produce hydroxyl radicals from H_2O_2 to oxidize MC-LR is presented in Fig. 11.

CuO-NPAC$_{400}$ acts as a heterogeneous catalyst to facilitate the sequential adsorption and destruction of MC-LR by the following proposed mechanism. The generation of hydroxyl radicals from CuO-NPAC and hydrogen peroxide system is illustrated in reactions (1) and (2):

$$CuO-NPAC(h_{vb}^{+})+H_2O_2 \rightarrow CuO-NPAC^{*}(^{\bullet}OH)_{ads}+OH_{aq}^{-} \quad (1)$$

$$CuO-NPAC^{*}(h_{vb}^{+})+H_2O_2 \rightarrow CuO-NPAC(^{\bullet}OOH)_{ads}+H_{aq}^{+} \quad (2)$$

MC-LR is oxidized by CuO/NPAC-H_2O_2 system while oxygen was supplied to facilitate the degradation process. Molecular oxygen adsorbed on CuO-NPAC can generate reactive oxygen species by free electron on the surface of CuO-NPAC matrix.

$$CuO-NPAC(e_{cb}^{-})+O_2 \rightarrow CuO-NPAC^{*}(^{\bullet}O_2)_{ads} \quad (3)$$

Hydroxyl radicals react with adsorbed MC-LR on the CuO-NPAC matrix and degrade it gradually into smaller fragments as shown in reactions (4) and (5)

$$CuO-NPAC(h_{vb}^{+})+MC-LR \rightarrow CuO-NPAC^{*}(MC-LR^{+})_{ads} \quad (4)$$

$$CuO-NPAC^{*}(MC-LR^{+})_{ads} \rightarrow CuO-NPAC(h_{vb}^{+})+\text{Oxidized product}+e_{cb}^{-}+energy \quad (5)$$

Where, h_{vb}^{+} is the electron hole in the valence band; e_{cb}^{-} is the electron in the conduction band; CuO-NPAC* refers to the electron transfer site.

Based on the accepted heterogeneous Fenton oxidation reaction, hydroxyl radicals are generated from the CuO sites in the NPAC matrix. The MC-LR can react with

CuO/NPAC-H_2O_2 system to form fragmented compounds which is confirmed from the LC-MS spectrum. These fragmented compounds can further undergo hydroxylation in the presence of excess hydroxyl radicals to form smaller non-toxic molecules as presented in Fig S5 (a, b). Taking into account of the previous proposed degradation mechanisms [57, 58], we summarize the possible degradation products in Fig. 12.

One of the most intense peak (m/z) at 1029 observed in the LC-MS spectrum, this proposed that in addition of dihydroxylated product (4 and 5 or 6 and 7 dihydroxy); the geometrical isomers of dihydroxy MC-LR could be deduced, where the diene structure had either (4E),6(Z) or 4(Z),6(E) adda-MC-LR. Hydroxyl radical addition on the diene double bonds were frequently reported by researchers [59, 60]. The dihydroxylated MC-LR underwent further oxidation to cleavage dihydroxylated bond of adda side chain at position of 4-5 or 6-7. This is confirmed by the observation of cleavage products with m/z values at 795 and 835 [61-63]. This would suggest that the unsaturated bonds on the adda group are most vulnerable to attack by hydroxyl radical generated from CuO-NPAC matrix. The formation of m/z at 965, which is linearized product of MC-LR, can be attributed to cleavage of peptide bond between mdha and ala group of MC-LR. LC-MS spectrum showed one fragment with m/z 617 corresponding to Mdha and MeAsp-Arg peptide ring. The peptide ring undergoes hydrolyzation and cleaves to form a linearized product with the loss of Mdha-Ala-Leu-MeAsp peptides, which is a linearized product of MC-LR.

The linearized product with Adda side chain may be the result of hydroxyl radical attack to form the hydroxylated product with m/z of 651. This may undergo cleavage of the hydroxylated adda bond to form low molecular weight compounds. Earlier reports by Joel *et al.* (2014) stated that the m/z 793.53 fragment, produced by the intact Adda amino acid is free from toxicity [4]. This confirmed results from cell line

toxicity studies of MC-LR. It was observed that the final product did not affect the cell line after treatment with CuO-NPAC catalyst as shown in Fig. 12. However, the identification of the complete list of degradation products is still under study.

Conclusions

In the present study, nanoporous activated carbon supported copper oxide catalysts were prepared by annealing at 300, 400 and 500 ^{o}C, and varying the copper oxide loading. CuO-NPAC$_{400}$ exhibited the highest catalyst activity for MC-LR degradation. A critical evaluation of this catalyst as oxidative system in the presence of H_2O_2 proved that CuO-NPAC/H_2O_2 was an efficient catalytic system for the degradation of MC-LR in aqueous solution. The degradation efficiency was largely influenced by solution pH, and the concentrations of H_2O_2 and MC-LR. Hydroxyl radical generation was verified by EPR and HTPA trapping using both Fenton oxidation and CuO-NPAC systems. MC-LR degradation studies were performed at different pH, with MC-LR conversions of 98 %, 95.4 % and 94 % at pH 3, 7 and 9 respectively, after 80 min reaction. The degradation rate of MC-LR increased from $3.2x10^{-2}$ µg.min^{-1} to $5.6x10^{-2}$ µg.min^{-1} with increasing initial MC-LR concentration from 10 µg.L^{-1} to 100 µg.L^{-1}. A H_2O_2 concentration of 15 mM was required to effect MC-LR degradation by the CuO-NPAC catalyst. Negligible copper leached from the carbon matrix during the heterogeneous Fenton oxidation process. Our study shows that CuO-NPAC catalyses hydroxyl radical-based heterogeneous Fenton-like processes to degrade MC-LR and thereby form a variety of reaction intermediates. Such properties make CuO-NPAC a promising catalyst for rapid and low cost water treatment via a Fenton-like process.

Notes

The authors declare no competing financial interest.

Acknowledgements

One of the author (S.K) acknowledges CSIR, India (grant number 31/6(365)/2012-EMR-I) for Senior Research Fellowship. The financial assistance under SETCA network programme to carry out this work is highly acknowledged. D. D. Dionysiou also acknowledges support from the University of Cincinnati through a UNESCO co-Chair Professor position on "Water Access and Sustainability". A.F.L. thanks the EPSRC (EP/G007594/4) for the award of a Leadership Fellowship. KW thanks the Royal Society for an Industry Fellowship.

Supporting Information

Fig. S1 (a) Pore size distribution vs. pore diameter of NPAC and CuO-NPAC, (b) XPS spectrum of CuO-NPAC annealed at 500 °C, Fig. S2 (a) The generation hydroxyl radicals was verified by spin trap technique using Fenton oxidation process, (b) shows generation of hydroxyl radical using CuO-NPAC with hydrogen peroxide, Fig. S3 (a) Photoluminescence spectrum of NPAC, (b) CuO-NPAC, Table S1 Effect of CuO weight percentage on NPAC and leaching of copper after MC-LR oxidation, Fig. S4 TPA and HTPA fluorescence spectroscopy at different time interval. Fig. S5 (a) LC-MS spectrum of MC-LR, Fig. S5 (b) LC-MS spectrum of intermediates of MC-LR (m/z at 1029).

References

1. E. H. Hashimoto, H. Kato, Y. Kawasaki, Y. Nozawa, K. Tsuji, E. Y. Hirooka, and K. Harada, *Chem. Res. Toxicol.,* 2009, **22**, 391–398.

2. W. Song, T. Teshiba, K. Rein, and K. E. O'Shea, *Environ. Sci. and Technol.,* 2005, **39**, 6300-6305.

3. R. A. Halvorson, P. J. Vikesland, Environ. Sci. and Technol., 2011, **45,** 5644-5651.

4. J. Andersen, C. Han, K. O'Shea, D. D. Dionysiou, *Appl. Catal. B: Environ.,* 2014, **154–155,** 259–266.

5. M. Pelaez, B. Baruwati, R. S. Varma, R. Luque, D. D. Dionysiou, *Chem. Commun.,* 2013, **49,** 10118-10120.

6. M. Pelaez, P. Falaras, A. G. Kontos, A. A. Cruz, K. O'Shea, P. S. M. Dunlop, J. A. Byrne and D. D. Dionysiou, *Appl. Catal. B: Environ.,* 2012, **121,** 30–39.

7. F. Al Momani, D. W. Smith, M. Gamal El-Din, *J. Hazard. Mater.,* 2008, **150** 238-249.

8. N. M. Bedford, M. Pelaez, C. Han, D. D. Dionysiou, A. J. Steckl, *J. Mater. Chem.,* 2012, **22,** 12666-12674.

9. T. M. Triantis, T. Fotiou, T. Kaloudis, A. G. P. Kontos, Falaras, D. D. Dionysiou, A. Hiskia, *J. Hazard. Mater.,* 2012, **211,** 196-202.

10. J. Rositano, G. Newcombe, B. Nicholson, P. Sztajnbok, *Water Res.,* 2001, **35,** 23–32.

11. J. Chang, Z. L. Chen, Z. Wang, J. M. Shen, Q. Chen, J. Kang, C. X. Nie, *Water Res.,* 2014, **63,** 52-61.

12. J. J. Pignatello, E. Oliveros, A. MacKay, *Crit. Rev. Env. Sci. Technol.,* 2006, **36,** 1–84.

13. C. Bradu, L. Frunza, N. Mihalche, S. M. Avramescu, M. Neaţa, I. Udrea, *Appl. Catal. B: Environ.,* 2010, **96,** 548-556.

14. J. Liao, H. Li, X. Zhang, D. Xiao, N. Qiang, *Appl. Catal. A: General,* 2015, **491,** 94-99.

15. L. Parimala, J. Santhanalakshmi, *Reaction Kinetics, Mechanisms and Catalysis,* 2013, **109,** 393-403.

16. W. Pan, G. Zhang, T. Zheng, P. Wang, RSC Advances, 2015, **5,** 27043-27051.

17. S. Karthikeyan and G. Sekaran, *Phys. Chem. Chem. Phys.,* 2014, **16,** 3924-3933.

18. S. Karthikeyan, A. Titus, A. Gnanamani, A. B. Mandal, G. Sekaran, *Desalination,* 2011, **281,** 438–445.

19. G. Sekaran, S. Karthikeyan, R. Boopathy, P. Maharaja, V. K. Gupta, C. Anandan, *Environ. Sci. Pollution Res.,* 2014, **21,** 489-1502.

20. S. Karthikeyan, V. K. Gupta, G. Sekaran, *Environ. Sci. Pollut. Res.,* 2013, **20,** 4790–4806.

21. S. Karthikeyan, C. Judia Magthalin and A. B. Mandal, G. Sekaran, *RSC Advances* 2014, **4,** 19183-19195.

22. Y. Chang Hun, Y. H. Park, C. R. Park, *Carbon* 2001, **39,** 559.

23. X. Hu, L. Lei, H. P. Chu, P. L. Yue, *Carbon*, 1999, **37,** 631-637.

24. R. Malik, D. S. Ramteke, S. R. Wate, Waste Manage., 2007, **27**, 1129-1138.

25. Y. F. Jia, K. M. Thomas, *Langmuir,* 2000, **16,** 1114-1122.

26. G. G. Stavropoulos, P. Samaras, G. P. Sakellaropoulos, *J. Hazard. Mater.,* 2008, **151** 414-421.

27. S.H. Park, W.J. Lee, *2015. Nature Sci. Reports* Doi: 10.1038/srep09754.

28. B. Zhao, P. Liu, H. Zhuang, Z. Jiao, T. Fang, W. Xu, Y. Jiang, *J. Mater. Chem. A,* 2013, **1,** 367-373.

29. S. Y. Lee, N. Mettlach, N. Nguyen, Y .M. Sun, J. M. White, *Appl. Surf. Sci.***,** 2003, **206,** 102–109.

30. M. R. Johan, M. S. M. Suan, N. L. Hawari, H. A. Ching, *Int. J. Electrochem. Sci.,* 2011, **6,** 6094-6104.

31. U. Aruldoss, L. J. Kennedy, J. Judith Vijaya, G. Sekaran, *J. Colloid. Interface Sci.***,** 2011, **355,** 204-209.

32. M. P. Pachamuthu, V. V. Srinivasan, R. Maheswari, K. Shanthi, A. Ramanathan, Catal. Sci. Technol., 2013, **3,** 3335-3342.

33. P. Fu, Y. Luan, X. Dai, *J. Mol. Catal. A: Chem.*, 2004, **221,** 81–88.

34. G. Socrates, John Wiley and Sons, England, 1994.

35. S. Safa, R. Azimirad, S. Safalou Moghaddam, M. Rabbani, *Desalin. Water Treat.,* 2015, 1-9.

36. S. Magdassi, M. Grouchko, A. Kamyshny, *Materials,* 2010, **3,** 4626-4638.

37. P. Wang, Y. Tang, Z. Dong, Z. Chen, T. T. Lim, *J. Mater. Chem A.,* 2013, **1,** 4718-4727.

38. Y. Zhao, X. Song, Q. Song, Z. Yin, *CrystEngComm,* 2012, **14,** 6710-6719.

39. H. Jiang, L. Huang, Z. Zhang, T. Xu, W. Liu, *Chem. Commun.,* 2004, **19,** 2196-2197.

40. J. Chastain, R.C. King, Eds. Physical Electronics, Inc. Eden Prairie, MN, 1995, pp 80.

41. I. N. Kholmanov, S. H. Domingues, H. Chou, X. Wang, C. Tan, J. Y. Kim, and R. S. Ruoff, *ACS Nano,* 2013, **7,** 1811-1816.

42. Christopher J. Rhodes, Electron spin resonance, *Annu. Rep. Prog. Chem., Sect. C,* 2011, **107,** 47–87.

43. S. Yu, H. J. Yun, D. M. Lee and J. Yi, *J. Mater. Chem.,* 2012, **22,** 12629-12635.

44. A. G. Pandolfo, A. F. HollenKamp, *J. Power Sour.,* 2006, **157,** 11-27.

45 J. Liqiang, Q. Yichun, Baiqi, W., Shudan, L., Baojiang, J., Libin, Y., Jiazhong, S. *Sol. Energ. Mat. Sol. C.,* 2006, **90,** 1773-1787.

46. K. Y. Foo, B. H. Hameed, *Adv. Colloid Interface Sci.,* 2010, **159,** 130–143.

47. E. Bourelle, Y. Kaburagi, Y. Hishiyama, M. Inagaki, *Carbon,* 2001, **39,** 1955–1962.

48. E. R. Bandala, D. Martınez, E. Martınez, D. D. Dionysiou, *Toxicon,* 2004, **43,** 829–832.

49. P. Gajdek, Z. Lechowski, T. Bochnia, M. Kepczynski, *Toxicon,* 2001, **39,** 1575–1578.

50. F. Wang, Y. Gao, Q. Sun, Z. Chen, M. Megharaj, R. Naidu, *Chem. Eng. J.,* 2014, **255,** 55-62.

51. C. L. Hsueh, Y. H. Huang, C. C. Wang, *Chemosphere,* 2005, **58,** 1409-1414.

52. H. Selçuk, G. Eremektar, S. Meriç, *J. Hazard. Mater.,* 2006, **137,** 254–260.

53. S. Wang, *Dyes and Pigments* 2008, **76,** 714-720.

54. F. J. Rivas, S. T. Kolaczkowski, F. J. Beltran, D. B. Mc Lurgh, *J. Chem. Technol. Biotechnol.***,** 1999, **74,** 390–398.

55. S. Karthikeyan, C. Judia Magthalin, M. Mahesh, C. Anandan, G. Sekaran, *J. Chem. Technol. Biotechnol.* 2014, **90,**1013-1026.

56. S. Kanazawa, T. Furuki, T. Nakaji, S. Akamine, R. Ichiki, In J. Phy. Conference Series 2013, **418,** 012-102.

57. M. G. Antoniou, J. A. Shoemaker, A. A. D. L. Cruz, D. D. Dionysiou, *Environ. Sci. and Technol.* 2008, **42,** 8877-8883.

58. I. Liu, L. A. Lawton, P. K. Robertson, *Environ. Sci. Technol.*, 2003, **37,** 3214-3219.

59. H. F. Miao, F. Qin, G. J. Tao, W. Y. Tao, W. Q. Ruan, *Chemosphere,* 2010, **79,** 355-361.

60. I. C. Lopes, P. V. Santos, V. C. Diculescu, F. M. Peixoto, M. C. Araújo, A. A. Tanaka, A. M. Oliveira-Brett, *Analyst,* 2012, **137,** 1904-1912.

61. W. Song, A. A. De La Cruz, K. Rein, K. E. O'Shea, *Environ. Sci. and Technol.*, 2006, **40,** 3941-3946.

62. Su, Y., Deng, Y., & Du, Y. *J. Mol. Catal. A: Chem.*, 2013, **373,** 18-24.

63. X. He, A. Armah, A. Hiskia, T. Kaloudis, K. O'Shea, D. D. Dionysiou, *Water Res.,* 2015, **74**, 227-238.

Table 1 BET surface area and pore diameters of NPAC and CuO-NPAC

Sample	NPAC	CuO-NPAC$_{300}$	CuO-NPAC$_{400}$	CuO-NPAC$_{500}$
BET surface area ($m^2.g^{-1}$)	153	128	99	154
S_{meso} ($m^2.g^{-1}$)	119	84	77	95
S_{micro} ($m^2.g^{-1}$)	34	44	22	59
Total pore volume ($cm^3.g^{-1}$)	0.19	0.13	0.11	0.14
V_{micro} ($cm^3.g^{-1}$)	0.017	0.019	0.010	0.026
V_{meso} ($cm^3.g^{-1}$)	0.17	0.11	0.10	0.11
Mean pore diameter (nm)	5.0	4.1	4.6	3.7

Table 2 Elemental composition of NPAC and CuO-NPAC

Mass (mg)	Name	N (%)	C (%)	H (%)	S (%)	C/N ratio	C/H ratio	CuO wt.%
4.20	NPAC	1.84	41.48	1.44	0.11	22.50	28.62	-
3.89	CuO-NPAC $_{300}$	1.01	32.14	1.10	0.15	31.72	29.11	0.91
3.16	CuO-NPAC $_{400}$	1.04	33.54	1.39	0.27	32.06	23.99	0.94
3.94	CuO-NPAC $_{500}$	0.88	32.82	1.13	0.17	37.04	28.89	0.93

Table 3 EPR g-factor for synthesised NPAC and CuO-NPAC catalyst

Sl No.	Catalyst	g value	Correction factor
1	NPAC	2.0138, 0.0138	0.9970
2	CuO-NPAC$_{300}$	2.0085, 2.3478	0.9970
3	CuO-NPAC$_{400}$	2.0048, 2.3958	0.9970
4	CuO-NPAC$_{500}$	2.0065, 2.3972	0.9970
5	CuO-NPAC (0.1%)	2.0076, 2.3951	0.9970
6	CuO-NPAC (0.5%)	2.0085, 2.3812	0.9970
7	CuO-NPAC (1.0%)	2.0076, 2.3964	0.9970
8	CuO-NPAC (1.5%)	2.0066, 2.3312	0.9970
9	CuO-NPAC (2.0%)	2.0060, 2.3910	0.9970

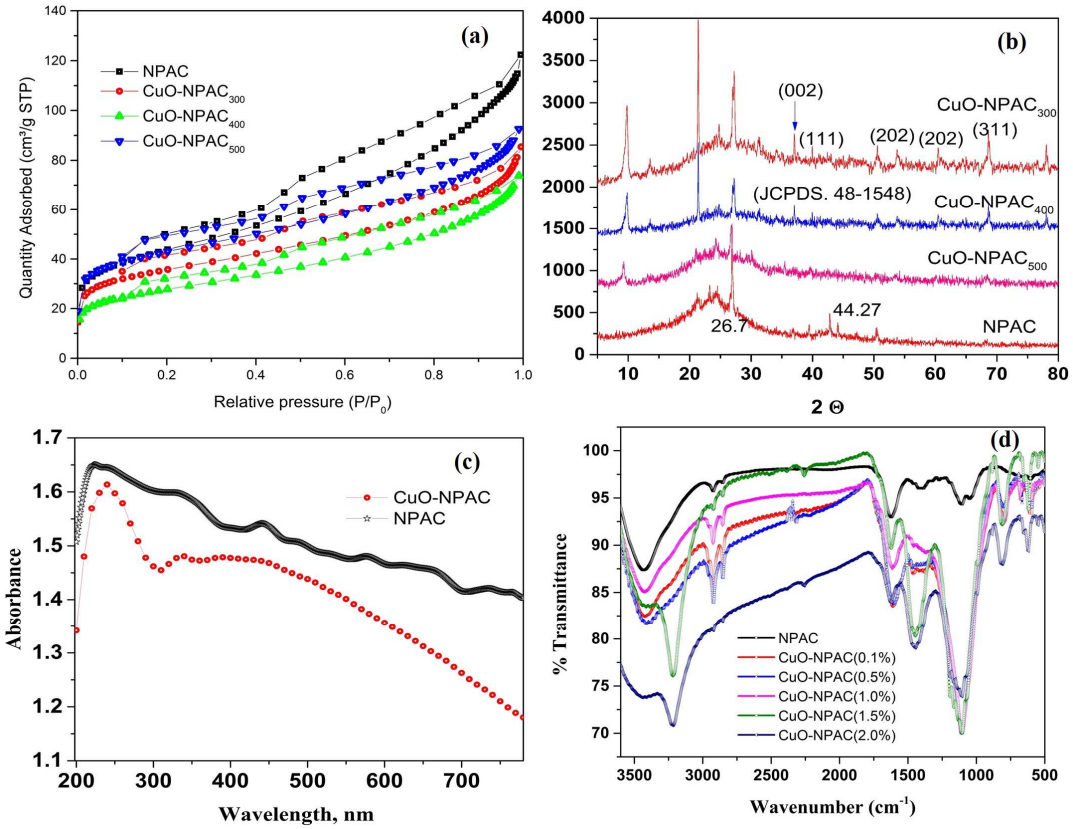

Fig. 1 (a) Nitrogen Adsorption–Desorption Isotherms of NPAC and CuO-NPAC, (b) XRD patterns of NPAC and CuO-NPAC, (c) DRS-spectrum of NPAC and CuO-$NPAC_{400}$, (d) FTIR spectra of NPAC and CuO-$NPAC_{400}$ at different weight percentage.

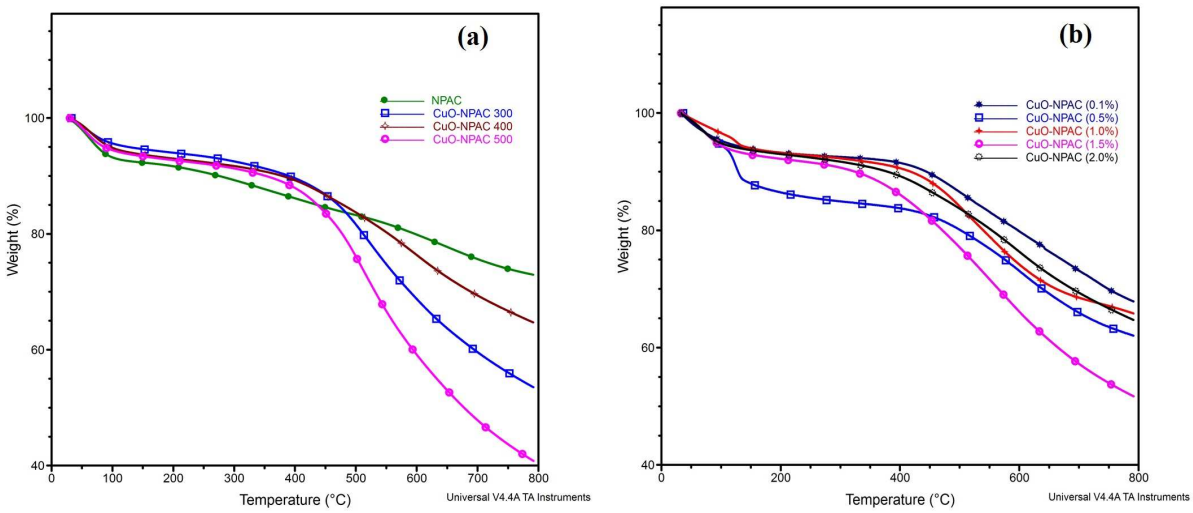

Fig. 2 (a) TGA profiles of NPAC and CuO-NPAC, (b) TGA profiles of CuO-NPAC$_{400}$

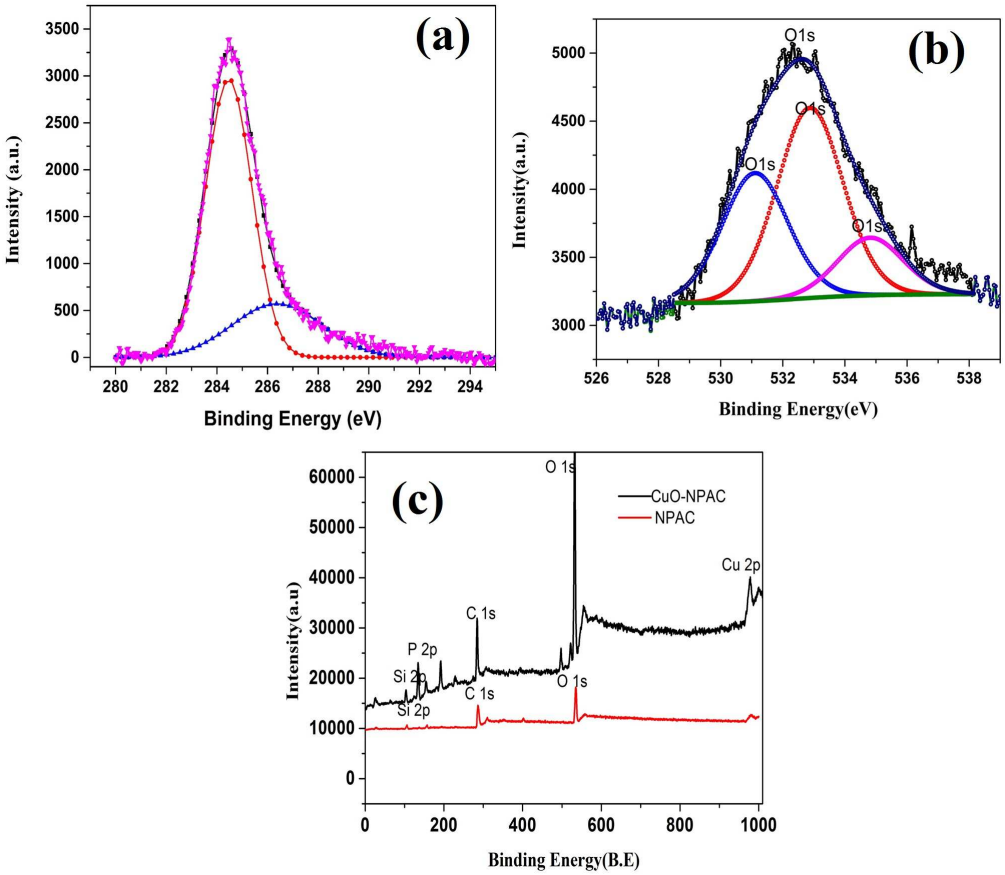

Fig. 3 (a) XPS spectra of C1s core level spectra for NPAC and CuO-NPAC, (b) O1s binding, (c) XPS binding energy of C1s, O 1s, N 1s, Cu 2p and Si 2p for NPAC and CuO-NPAC

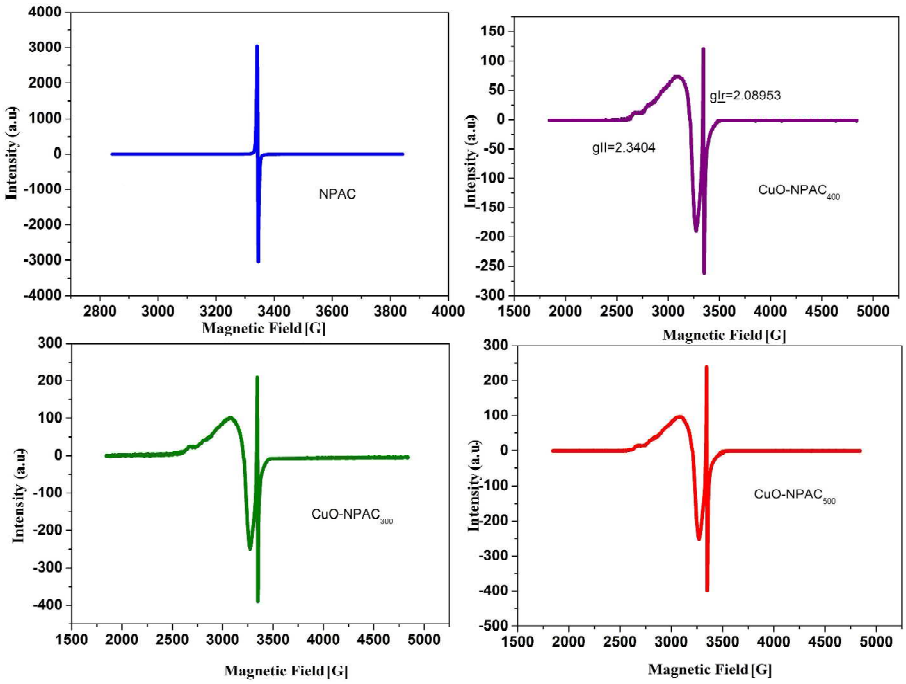

Fig. 4 EPR spectroscopy of NPAC and CuO-NPAC at different annealing temperatures

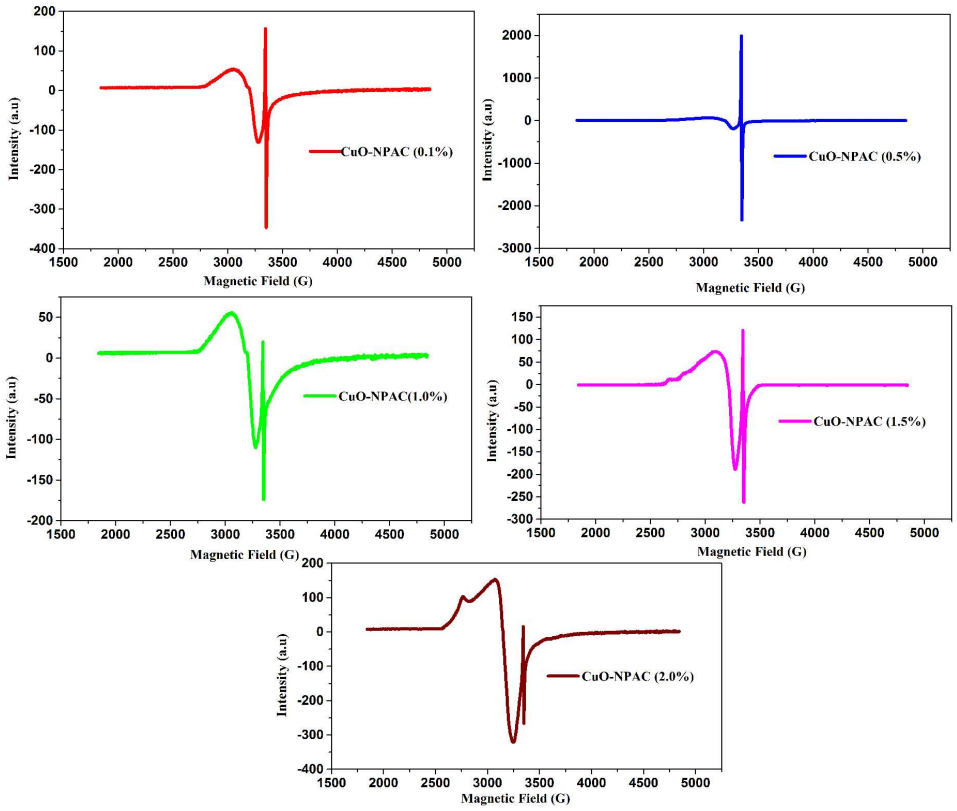

Fig. 5 EPR spectra of CuO-NPAC at different loading of CuO

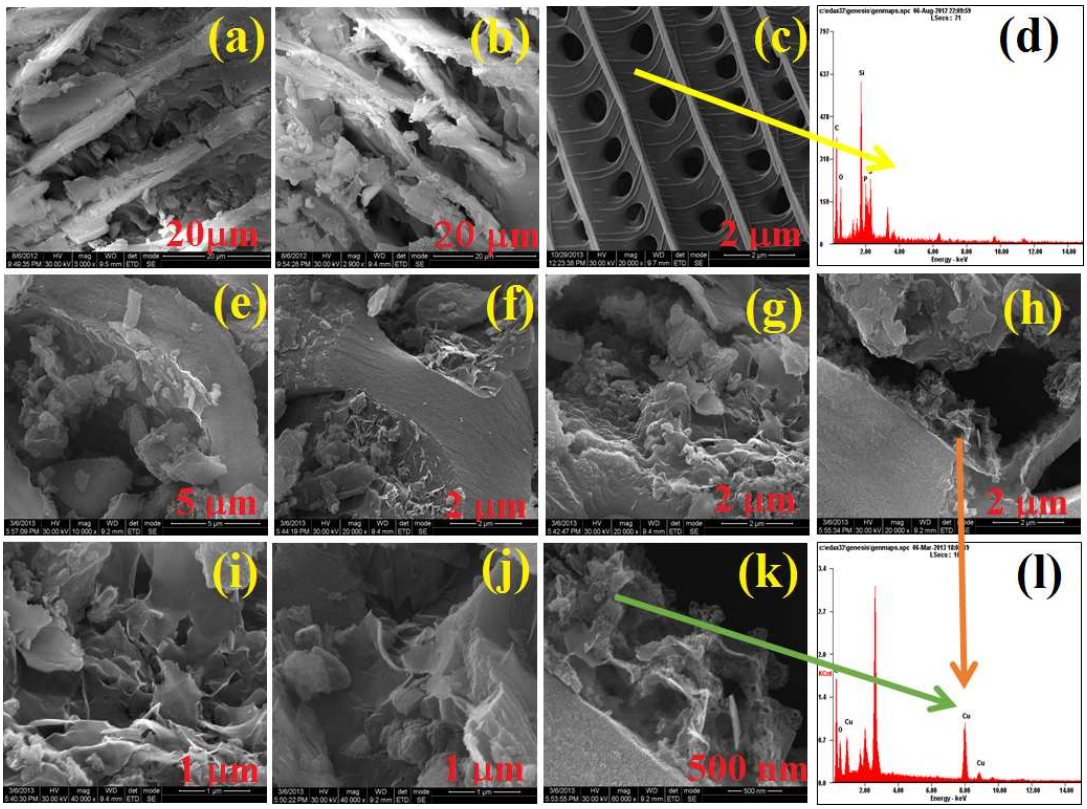

Fig. 6 (a- c) SEM images of NPAC, (d) EDX spectrum of NPAC, (e-k) HR-SEM images of CuO-NPAC$_{400}$, (l) EDX analysis of CuO-NPAC$_{400}$

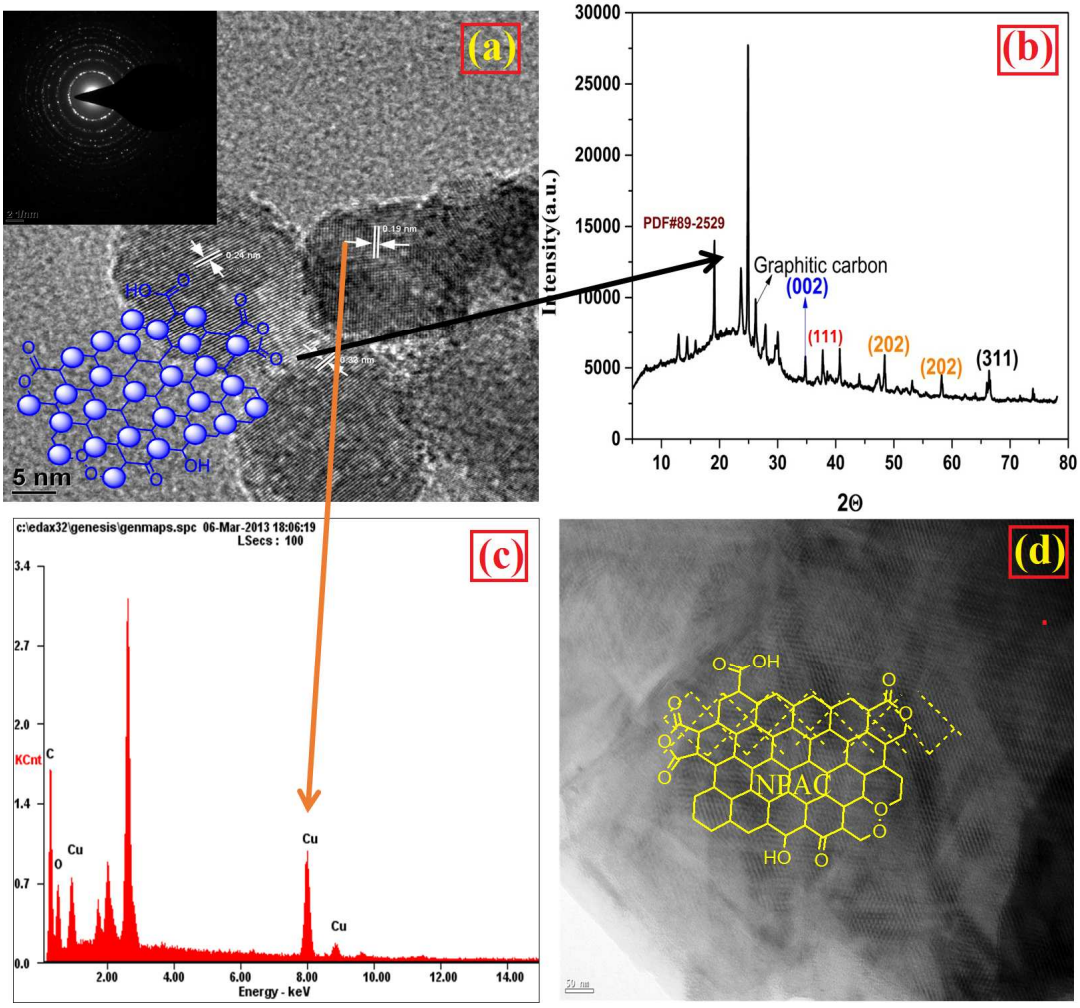

Fig. 7 (a) HR-TEM image of CuO-NPAC$_{400}$, (a) SAED pattern of CuO-NPAC$_{400}$ (left inserted), (b) XRD pattern of CuO- NPAC$_{400}$, (c) EDX analysis of CuO-NPAC$_{400}$, (d) HR-TEM image of NPAC

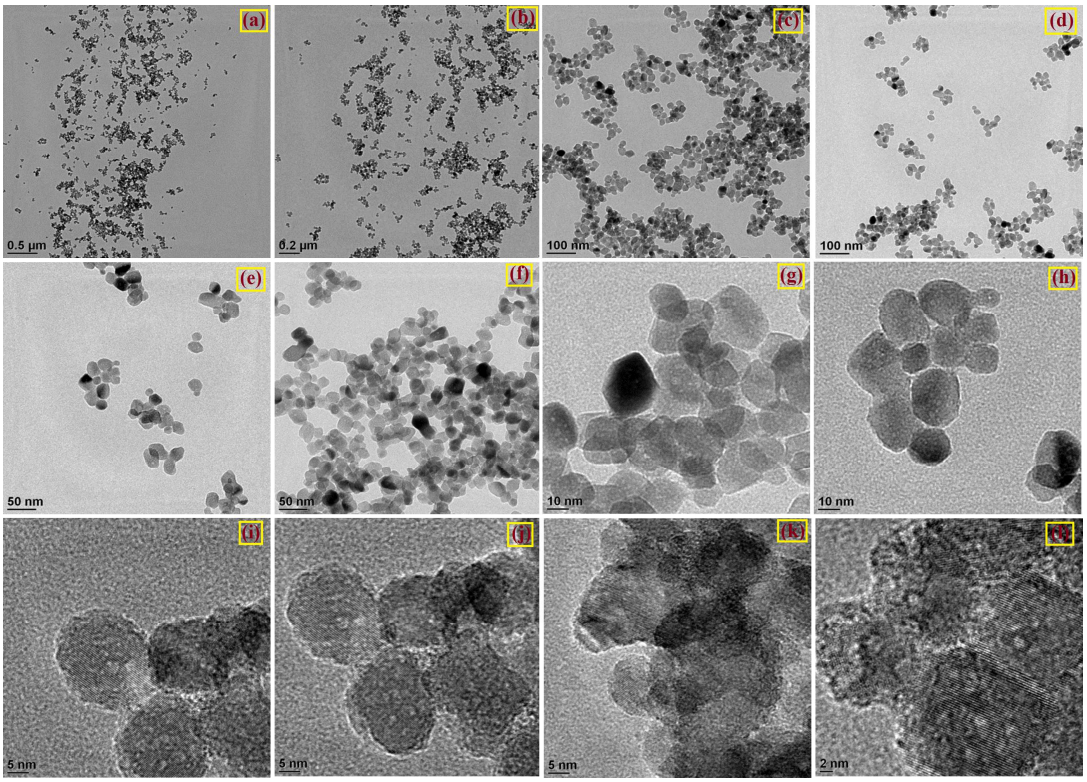

Fig. 8 (a-l) HR-TEM images of CuO-NPAC$_{400}$

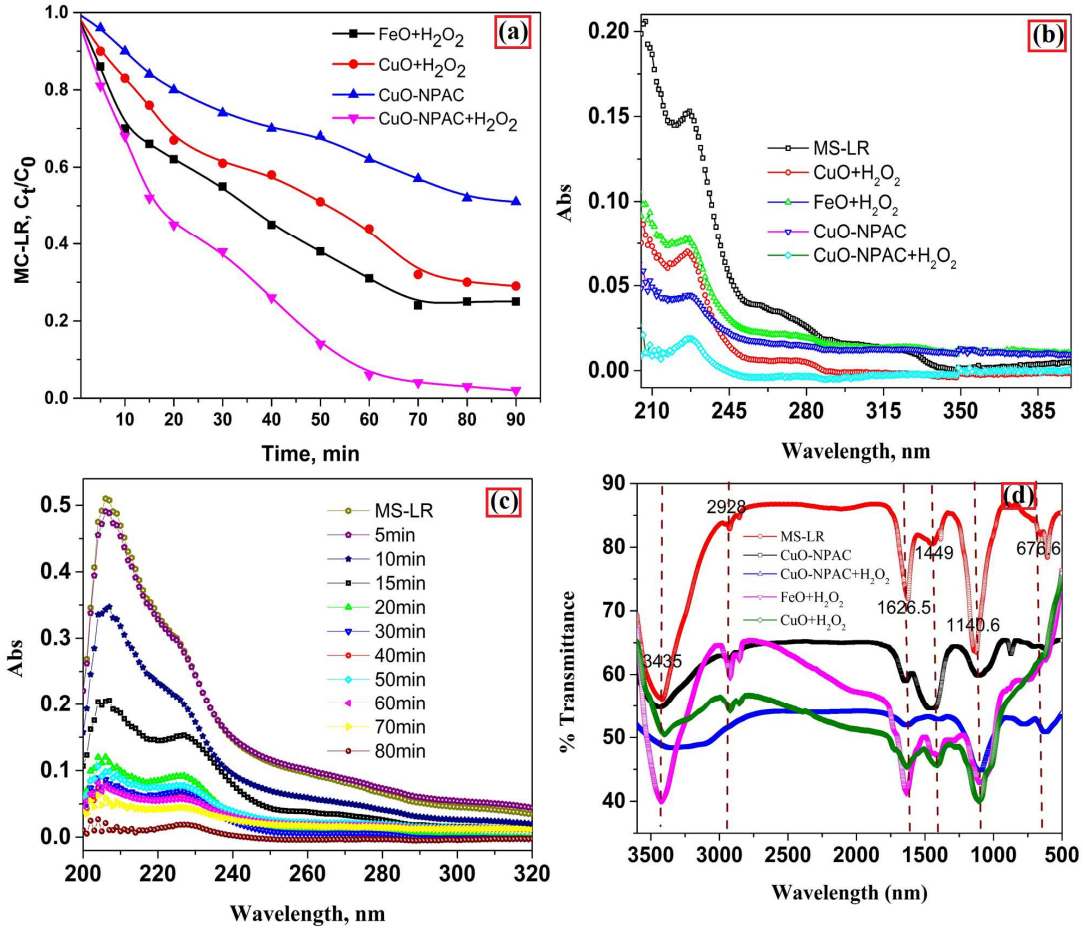

Fig. 9 (a) MC-LR degradation over CuO-NPAC$_{400}$ alone, homogeneous Fenton oxidation using [FeO with H_2O_2), CuO with H_2O_2)], and heterogeneous Fenton oxidation process using CuO-NPAC$_{400}$ with H_2O_2, (b) UV-Vis spectra of MC-LR degradation over the CuO-NPAC$_{400}$ alone, homogeneous Fenton oxidation using [(FeO with H_2O_2), CuO with H_2O_2)], and heterogeneous Fenton oxidation process using CuO-NPAC$_{400}$ with H_2O_2, (c) UV-Vis spectra of MC-LR degradation at different time intervals (heterogeneous Fenton oxidation), (d) FT-IR spectra of MC-LR degradation over CuO-NPAC$_{400}$ alone

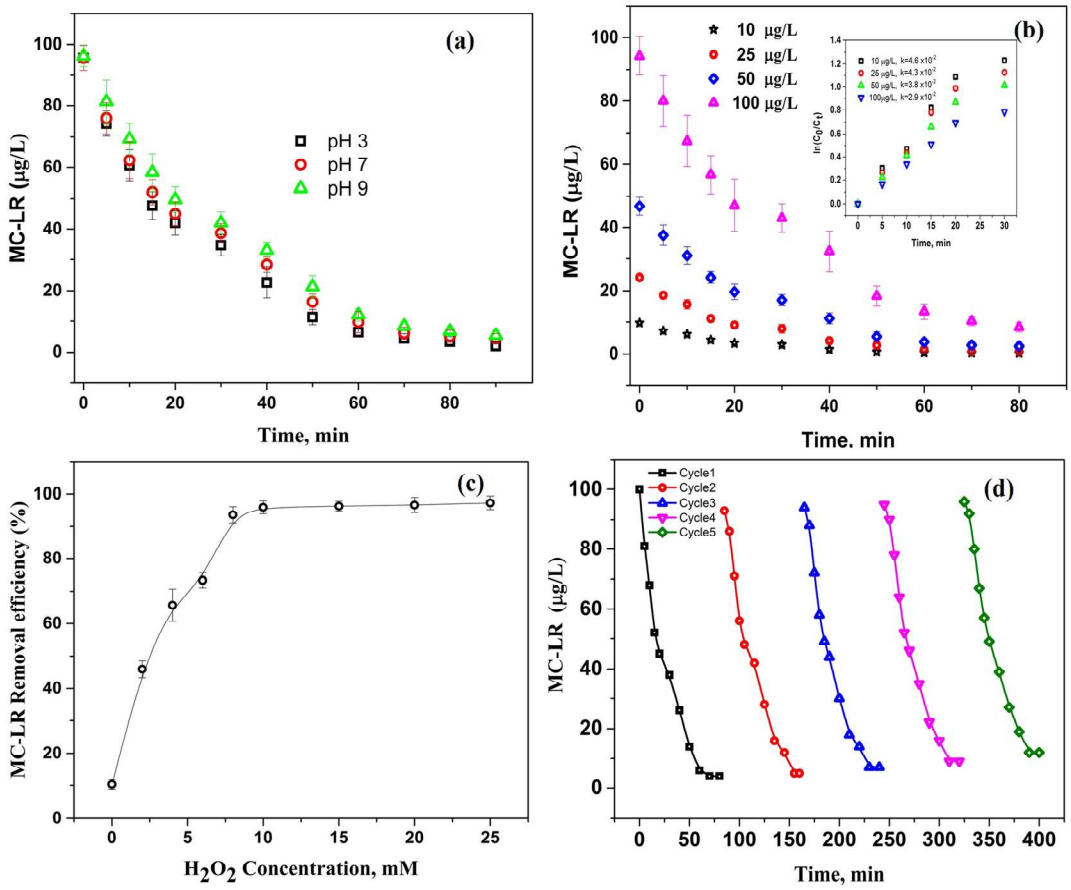

Fig.10 (a) Effect of pH on the degradation of microcystin-LR; conditions: microcystin-LR, 50 µg/L; CuO-NPAC, 2 g/L; H_2O_2, 15 mM; (b) Effect of Microcystin-LR ; CuO-NPAC- H_2O_2 oxidation; conditions: pH, 7.0; CuO-$NPAC_{400}$, 2 g/L; H_2O_2, 15 mM; (c) Effect of H_2O_2 on degradation of microcystin-LR; conditions: microcystin-LR, 50 µg/L; CuO-$NPAC_{400}$, 2 g/L; pH, 7.0; Reaction time, 80 min, (d) Stability of CuO-$NPAC_{400}$

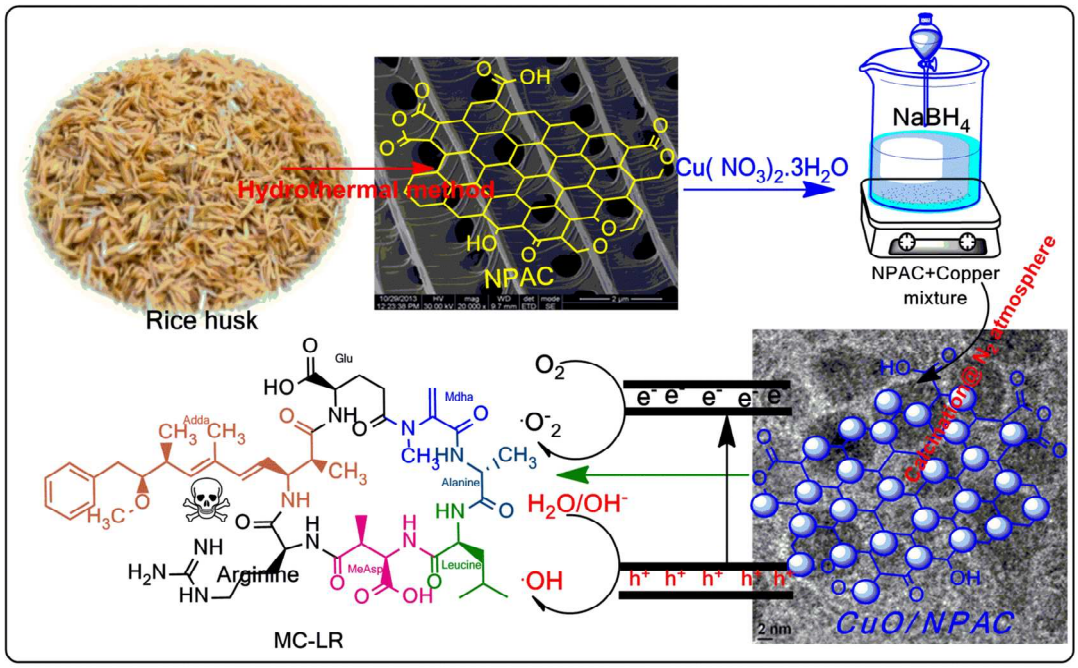

Fig. 11 Graphical representation for the generation of hydroxyl radical

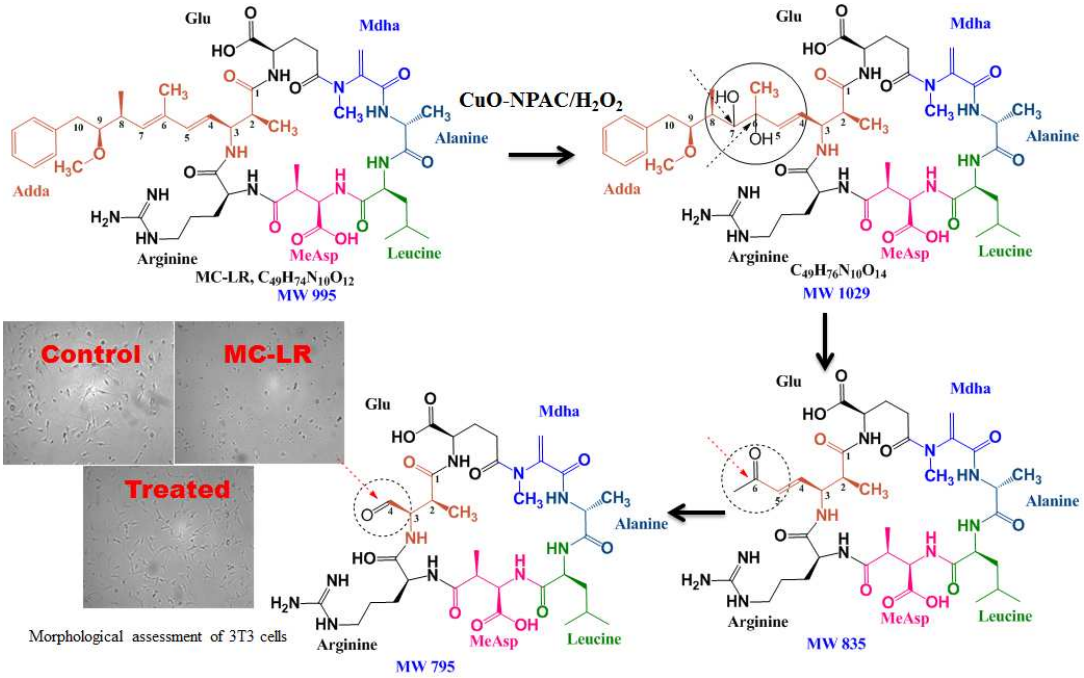

Fig.12 Degradation byproducts of MC-LR